Changes in stratospheric aerosol extinction coefficient after the 2018 Ambae eruption as seen by OMPS-LP and ECHAM5-HAM

Elizaveta Malinina[1*], Alexei Rozanov[1], Ulrike Niemeier[2], Sandra Peglow[3], Carlo Arosio[1], Felix Wrana[3], Claudia Timmreck[2], Christian von Savigny[3], and John P. Burrows[1]

[1]Institute of Environmental Physics (IUP), University of Bremen, Bremen, Germany
[2]Max-Planck Institute for Meteorology, Hamburg, Germany
[3]Institute of Physics, University of Greifswald, Greifswald, Germany
[*]now at the Canadian Centre for Climate Modelling and Analysis (CCCma), Environment and Climate Change Canada, Victoria, Canada

Correspondence: Alexei Rozanov (alex@iup.physik.uni-bremen.de)

Abstract. Stratospheric aerosols are an important component of the climate system. They not only change the radiative budget of the Earth but also play an essential role in ozone depletion. Most noticeable those effects are after volcanic eruptions when SO_2 injected with the eruption reaches the stratosphere, oxidizes and forms stratospheric aerosol. There have been several studies, where a volcanic eruption plume and the associated radiative forcing were analyzed using climate models. Besides,
5 volcanic eruptions were studied using the data from satellite measurements; however, studies combining both models and measurement data are rare. In this paper, we compared changes in the stratospheric aerosol loading after the 2018 Ambae eruption observed by satellite remote sensing measurements and by a global aerosol model. We use vertical profiles of aerosol extinction coefficient at 869 nm retrieved at IUP Bremen from OMPS-LP (Ozone Mapping and Profiling Suite - Limb Profiler) observations. Here, we present the retrieval algorithm as well as a comparison of the obtained profiles with those from
10 SAGE III/ISS (Stratospheric Aerosol and Gas Experiment III onboard International Space Station). The observed differences are within 25% for the most latitude bins, which indicates a reasonable quality of the retrieved limb aerosol extinction product. The volcanic plume evolution is investigated using both: monthly mean aerosol extinction coefficients and 10-day averaged data. The measurement results were compared with the model output from ECHAM5-HAM. In order to simulate the eruption accurately, we use SO_2 injections estimates from OMPS and OMI for the first phase of eruption and TROPOMI for the second
15 phase. Generally, the agreement between the vertical and geographical distribution of the aerosol extinction coefficient from OMPS-LP and ECHAM is quite remarkable, in particular, for the second phase. We attribute the good consistency between the model and the measurements to the precise estimation of injected SO_2 mass and height as well as through nudging to ECMWF reanalysis data. Additionally, we compared the radiative forcing (RF) caused by the increase of the aerosol loading in the stratosphere after the eruption. After accounting for the uncertainties from different RF calculation methods, the RFs from
20 ECHAM and OMPS-LP agree quite well. We estimate the tropical (20° N to 20° S) RF from the second Ambae eruption to be about -0.13 W/m^2.

Copyright statement. TEXT

1 Introduction

The importance of stratospheric aerosols in the climate system now well established. Stratospheric aerosols influence it both
25   directly and indirectly. Firstly, they change the radiative budget of the Earth by scattering back to space the incoming short-
wave solar radiation and, thereby, cause a net negative radiative forcing (RF) (see, e.g., Thomason and Peter, 2006; Kremser
et al., 2016, and references therein). Secondly, stratospheric aerosols influence climate indirectly by participating in chemical
reactions which lead to ozone depletion (see, e.g., Solomon, 1999; Ivy et al., 2017; WMO, 2018).

Aerosols are present in the stratosphere all the time. Even though there is some evidence of a presence of organic particles,
30   soot, meteoritic dust as well as other solid particles in the stratosphere, the most abundant are the droplets of sulfuric acid with
a commonly assumed weight percentage of 75% H_2SO_4 and 25% H_2O. In the background state, stratospheric aerosols are
formed by continuous emissions of carbonyl sulfide (OCS), dimethyl sulfide (DMS) and other sulfuric gases from the ocean
surface. However, occasionally this state is perturbed. In recent years due to the increasing number of extreme weather events,
biomass burning became a significant source of stratospheric aerosols. Thus, during large biomass burning events, like the
35   Australian Bushfires of 2009 and 2019 (Siddaway and Petelina, 2011), as well as the Canadian Wildfires of 2017 (Khaykin
et al., 2018; Bourassa et al., 2019; Kloss et al., 2019), sulfuric gases and other combustion products are transported into the
stratosphere by convective clouds (pyrocumulonimbus). Another noticeable source of stratospheric sulfur is anthropogenic
fossil fuel combustion in South East Asia, where the aerosol precursors are transported into the stratosphere with the Asian
Monsoon (Randel et al., 2010). Although these sources are undoubtedly important, the large scale changes to the stratospheric
40   aerosol layer are primarily driven by moderate and large volcanic eruptions which emit sulfur dioxide (SO_2) directly into the
upper troposphere lower stratosphere (UTLS region (e.g. Kremser et al., 2016, and references therein).

Although volcanic eruptions are infrequent, they still significantly influence climate short and long-term. Consequently, it is
essential to consider them in climate models. According to Solomon et al. (2011); Haywood et al. (2014); Schmidt et al. (2018,
and references therein), it has been shown that climate models that neglect forcing from volcanic eruptions since the year
45   2000 tend to project a faster rate of global warming for the first 15 years of the 21st century than those models including this
volcanic forcing. There are numerous global aerosol model studies of historic and more recent eruptions. For example, several
papers focus on the June 1991 eruption of Mount Pinatubo (Niemeier et al., 2009; Feinberg et al., 2019; Dhomse et al., 2020).
Some studies also evaluate more recent moderate and small eruptions of the 21st century (e.g. Haywood et al., 2010; Kravitz
et al., 2010, 2011; Zhu et al., 2018; Lurton et al., 2018). Similarly, there are multiple studies which use measurement results to
50   analyze the changes in stratospheric aerosol loading either after some event (e.g., volcanic eruptions or biomass burning events)
(e.g., Siddaway and Petelina, 2011; Bourassa et al., 2019), or long term (e.g., Bingen et al., 2004; von Savigny et al., 2015;
Malinina et al., 2018). However, the studies which directly compare modelled and measured aerosol parameters are quite rare.
In the papers known to the authors, the monthly mean stratospheric aerosol optical depth (SAOD) was typically the parameter
used to compare models and measurements (e.g., Haywood et al., 2010; Kravitz et al., 2010, 2011; Lurton et al., 2018). Brühl

55 et al. (2018) used data from two satellite platforms and compared the vertically resolved aerosol extinction coefficient (Ext) at different wavelengths with model data in the period from 2002 to 2012. However, they compared spatial averages and did not focus on the plume distribution from volcanoes assessing agreement only in general terms.

  The scope of our study is to investigate the similarities and differences of how models and measurements show a volcanic plume evolution. For this reason, we use the time and altitude resolved Ext data retrieved from the limb viewing instrument

60 OMPS-LP and the output from the ECHAM model. We also study the differences in the modeled RF and that calculated from the measured data. Our study was conducted on the example of the 2018 Ambae eruption. This particular eruption was chosen because it was one of the strongest in the last decade; although, it did not receive as much attention as Kilauea eruption earlier that year or the 2019 Raikoke eruption.

  Ambae (or Aoba) island is located in the South Pacific in Vanuatu (15.39°S, 167.84°E): being a shield volcano with three

65 lakes in its caldera. According to Moussallam et al. (2019, and references therein), the previous significant Ambae eruption happened about 350 years ago; this information agrees with that from Smithsonian Institution (2019), according to which the active period of 2017-2018 was the strongest ever for this volcano. This period started on the 6 September 2017 and lasted over a year ending on the 30 October 2018. The researchers divide the eruption into four phases (Moussallam et al., 2019); however, for the stratospheric aerosol community, the most essential are the third and the fourth phases, when SO_2 was injected above

70 the tropopause. Namely, the third phase from mid-March to mid-April 2018, is associated with ash falls and acid rains, the largest SO_2 injection of the period occurred on the 6 April at 16-18 km altitude. However, the fourth phase in mid-July 2018 was more severe. Thus, on the 27 July 2018, along with ash, SO_2 was injected into the UTLS region (17 km). For consistency reasons, further in the text "the first" or "April eruption" refers to the third phase, and "the second" or "July eruption" defines the fourth phase.

75 The paper is structured as follows. In Sec. 2, the OMPS-LP instrument and its stratospheric aerosol retrieval algorithm are presented. The comparison of OMPS data with the data from SAGE III/ISS can be found in Sec. 3. The OMPS-LP aerosol extinction climatology is described in Sec. 4. The aerosol extinction coefficient distribution retrieved from the measurements made by the OMPS-LP instrument is presented in Sec. 5. The distribution of aerosol extinction coefficient as well as estimation of SO_2 mass from Ambae eruption is described in Sec. 6. Discussion of the results and the RF comparisons are presented in

80 Sec. 7. The conclusions of the paper are provided in Sec. 8.

2 OMPS-LP and Ext retrieval algorithm

There is only a limited number of methods to observe stratospheric aerosols, and the only option to obtain a global distribution of stratospheric aerosol profiles is to use space-borne measurements. While the first decade of the twenty-first century is known as the "golden era" of stratospheric observations with such instruments as the Stratospheric Aerosol and Gas Experi-

85 ment (SAGE) II, SAGE-III/Meteor (Damadeo et al., 2013), the SCanning Imaging Absorption SpectroMeter for Atmospheric CHartographY (SCIAMACHY) (Gottwald and Bovensmann, 2011), the Global Ozone Monitoring by Occultation of Stars (GOMOS) (Bertaux et al., 2004) and the Michelson Interferometer for Passive Atmospheric Sounding (MIPAS) (Fischer et al.,

2008) being on-orbit, nowadays there is a very limited number of space-borne missions, which can be used to retrieve strato-
spheric aerosol information. At the time of writing, only the Optical Spectrograph and InfraRed Imager System (OSIRIS)
90   (Llewellyn et al., 2004), the Cloud-Aerosol Lidar and Infrared Pathfinder Satellite Observations (CALIPSO) (Vernier et al.,
2011), the Ozone Mapping and Profiling Suite (OMPS) and the SAGE-III onboard International Space Station (ISS) continue
stratospheric aerosol measurements. At the same time, OSIRIS and CALIPSO launched in 2001 and 2006, respectively, are
now well beyond their intended lifetimes. Therefore, in this paper, in order to obtain stratospheric aerosol characteristics, we
use data from the OMPS instrument.

95   OMPS onboard Suomi National Polar-orbiting Partnership (SNPP) launched in late 2011 by NASA consists of three sensors:
nadir mapper (NM), nadir profiler (NP) and limb profiler (LP) (Seftor et al., 2014). To retrieve information on stratospheric
aerosols, only measurements from LP can be used.

OMPS-LP registers solar radiance scattered by the atmosphere. Unlike SCIAMACHY and OSIRIS, OMPS-LP does not use
a diffraction grating; instead, a prism disperses the light on a two-dimensional CCD (charge-coupled device) detector, which
100 registers the radiance simultaneously from all altitudes from 290 to 1000 nm with the spectral resolution from 1 nm to 30 nm
depending on the wavelength (Jaross et al., 2014). The LP has three vertical slits; however, we use only the measurements from
the central slit because of remaining pointing and stray-light issues on the side ones. Each slit registers vertically 105 pixels
with a 1.5 km instantaneous field of view of each detector pixel. The radiances are registered with a vertical sampling of 1 km
at the tangent point. The lowest and the highest registered altitudes vary depending on the latitude and season; nevertheless,
105 the altitude span from 5 to 80 km is constantly covered (Jaross et al., 2014).

As it can be inferred from its name, initially, OMPS was designed to obtain ozone products, and in the instrument design, the
UV-Vis parts of the spectrum were prioritized. As the prism dispersion is non-linear, the spectral resolution of the measurements
at the wavelength longer than 500 nm degrades exponentially, reaching about 30 nm at 1000 nm. This results in the situation
that the usual stratospheric aerosol extinction wavelength 750 nm, used by, e.g., SCIAMACHY and OSIRIS (Rieger et al.,
110 2018) is not suitable for use as OMPS-LP measurements around this wavelength are affected by the O_2-A absorption band.
Thus, for the stratospheric aerosol extinction retrieval, instead of 750 nm, we use the measurements at 869 nm (with a spectral
resolution of 22 nm), because the spectral interval from 830 to 900 nm is absorption free.

Even though some aspects of our algorithm have been briefly described in Arosio et al. (2018) and Malinina (2019), here,
we provide a consolidated summary. The OMPS V1.0.9 Ext_{869} retrieval algorithm was adapted from the SCIAMACHY V1.4
115 algorithm (Rieger et al., 2018) and uses the same regularized iterative approach. However, here, we use the first-order Tikhonov
regularization with the parameter value of 50 to smooth spurious oscillations in the level 1 V2.5 data. Based on the information
provided by NASA, the signal-to-noise ratio (SNR) is set to 500 for all the tangent altitudes.

In V1.0.9, Ext_{869} is retrieved on a 1 km grid from 10.5 to 33.5 km, with the measurement at 34.5 km being used as the refer-
ence. Additionally, the effective Lambertian albedo is simultaneously retrieved using the sun-normalized spectrum at 34.5 km.
120 The retrieval is done under the assumption of stratospheric aerosols being spherical sulfate droplets (75% H_2SO_4 and 25%
H_2O) with 0% relative humidity and unimodal lognormal particle size distribution. In this distribution the median radius (r_{med})
is equal to 0.08 μm and σ=1.6; the particle number density a priori profile is chosen in accordance with Extinction Coefficient

for STRatospheric Aerosol (ECSTRA) background climatology (Fussen and Bingen, 1999). We use the refractive indices from the OPAC database (Hess et al., 1998), for the selected wavelength the refractive index equals $1.425\text{-}1.38597 \times 10^{-7}i$. The

125   stratospheric aerosol profile is defined from 10 to 46 km; below and above, the number density profile is set to 0. After the retrieval, the Ext_{869} values higher than 0.1 km^{-1} are considered to be cloud contaminated and thus are filtered. Here we want to highlight, that we increased our threshold extinction value for the identification of cloud contamination (Malinina, 2019), because the previous threshold was filtering some profiles with increased aerosol loading.

3   OMPS extinction comparison with SAGE-III/ISS

130   ### 3.1   SAGE III/ISS instrument

Stratospheric Aerosol and Gas Experiment (SAGE) III on the International Space Station (ISS) started operating in early 2017 as a continuation of the SAM–SAGE data record. SAGE-III/ISS provides solar and lunar occultation, as well as limb-scatter measurements (Cisewski et al., 2014); however, for now, for stratospheric aerosol extinction coefficient retrievals, only solar occultation measurements are used. The principle of solar occultation is to measure solar irradiance attenuated by the Earth's

135   atmosphere between the Sun and the instrument during each sunrise and sunset. The solar occultation measurements are self-calibrating, and unlike limb instruments, for the Ext retrieval, no assumptions on the aerosol particle size distribution are needed, thus, making occultation measurements rather precise.

SAGE-III/ISS provides continuous measurements from 280 to 1040 nm with spectral resolution from 1 to 2 nm depending on the wavelength, which are registered on a 808×10 pixel CCD. Additionally, there is an infrared photodiode centered at 1550 nm

140   (McCormick et al., 2019, and references therein). According to Cisewski et al. (2014), the aerosol extinction coefficients provided by NASA have 0.75 km vertical resolution. In the official NASA product, aerosol extinctions are provided in 0.5 km steps from 0 to 45 km. Due to the ISS orbit, the measurements are performed from 70° N to 70° S. It should be noted here that occultation measurements are very sparse in comparison to limb measurements. This is because for one orbit a solar occultation instrument can register one sunrise and one sunset, while a limb instrument does not have these limitations. For

145   example, OMPS-LP provides 180 measurements per orbit, which drastically increases geographical sampling.

3.2   Comparison

The OMPS-LP Ext_{869} was originally retrieved to improve the ozone product (Arosio et al., 2018); however, it can also be used to evaluate the changes in stratospheric aerosol loading after volcanic eruptions and biomass burning events (Malinina, 2019). Here, it should be noted that there are three other OMPS aerosol extinction products. Two of them are the official NASA

150   Ext_{675} products V1.0 (Loughman et al., 2018) and V1.5 (Chen et al., 2018). Moreover, at the University of Saskatchewan, as a part of the ozone retrieval, a tomographic Ext_{750} product was obtained (Bourassa et al., 2019). All four Ext products were retrieved at different wavelengths and using different approaches. Thus, their inter-comparison will be challenging and will contain uncertainties, e.g., associated with Ångtröm exponent calculations.

In order to evaluate the quality of our Ext_{869}, it was compared with the SAGE III/ISS solar occultation product. There are

155   several advantages to this comparison. Firstly, SAGE III is an independent data set; thus, the OMPS instrumental uncertainties (e.g. scattering angle dependency) will not influence the comparison, as it would be with be the case for the other OMPS products. Secondly, SAGE III is an occultation instrument, which means that its Ext profiles are rather precise and independent of the aerosol PSD assumption, as, e.g., OSIRIS.

Another advantage of the comparison with SAGE III is the same measurement wavelength. Both, OMPS-LP and SAGE III

160   provide measurements at 869 nm, so aerosol extinction does not need to be recalculated assuming an Ångström exponent. Even though the spectral resolution of the instruments at this wavelength is different (1.5 nm in SAGE III versus 30 nm in OMPS-LP), it does not influence the aerosol extinction coefficient strongly because the wavelength interval from 830 to 900 nm is absorption free.

For the comparison, individual profiles from the 07 June 2017 until the 31 August 2019 were used. The profiles were

165   collocated using the following criteria, the difference between the profile's coordinates should be less than 2.5° in latitude, 10° in longitude and 24 hours in time. Overall, there are 19264 collocated measurements used for this comparison. For SAGE III data, the same as for OMPS, the aerosol extinction values higher than 0.1 km^{-1} were filtered out. Additionally, the SAGE III Ext_{869} values were excluded, if the uncertainty provided by NASA is higher than 50%. We did not filter negative Ext_{869} because this would bias the comparison.

170   The mean relative differences between OMPS and SAGE III Ext_{869} are presented in Fig. 1 in 20° latitude bins. For most of the altitudes in all latitude bins, the relative difference is within 25%. In the tropical and mid-latitudes, the only exceptions are the altitudes below 18 km, where despite filtering, the influence of clouds is still present. The largest differences are observed in high latitudes (40° to 80° in both hemispheres), in particular, at the altitudes above 24 km. For example, at about 28 km altitude, the differences reach up to 60% in these latitude bins.

175   Generally, the above-described differences are similar to the relative differences between SCIAMACHY V1.4, OSIRIS v5.07 and SAGE II v7 (Rieger et al., 2018; Malinina, 2019). Additionally, Chen et al. (2019) showed that the differences seen between OMPS Ext_{675} V1.5 and SAGE III product have the same shape and order of magnitude. Rieger et al. (2018) studied precisely the reasons for the seen differences. Since the OMPS V1.0.9 algorithm is very similar to the SCIAMACHY V1.4 algorithm used in that study, and since the OMPS and SCIAMACHY have very similar geometries, the same explanations as

180   Rieger et al. (2018) are appropriate. Thus, the most important sources of errors in limb retrievals arise from the uncertainly assumed aerosol loading at the reference tangent altitude as well as the unknown aerosol particle size distribution parameters. The latter factor mostly affects the high latitudes where the viewing geometries are close to forward and backward scattering.

Based on our comparison and the results from the other limb-occultation instrument studies, it can be concluded that our OMPS V1.0.9 Ext_{869} is of sufficient quality to be used for scientific purposes.
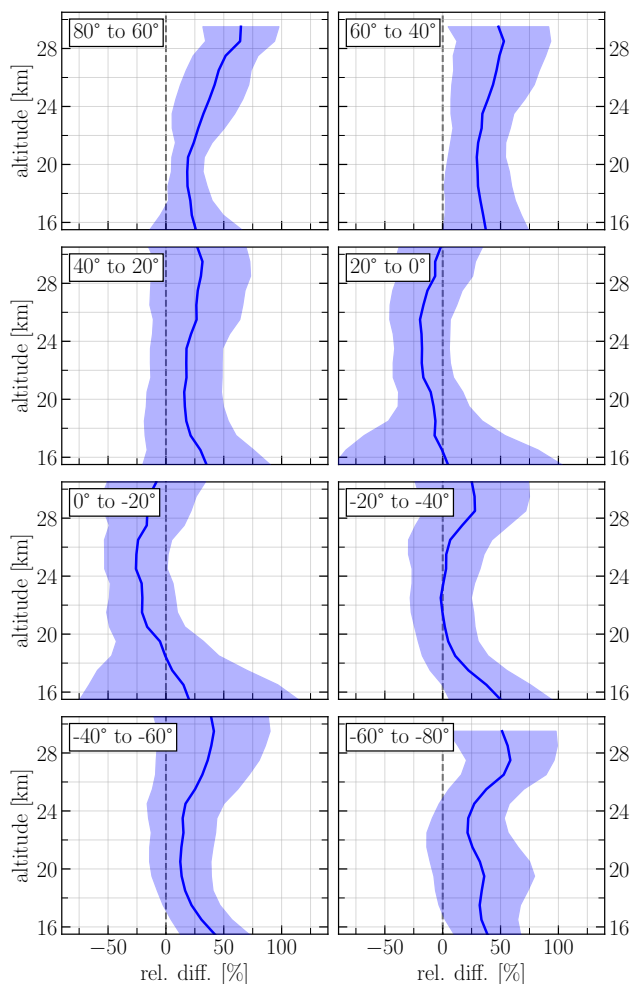
Figure 1. Mean relative difference in Ext_{869} between OMPS-LP and SAGE III/ISS, calculated as $200\times$(OMPS-SAGE)/(OMPS+SAGE). The shaded areas show $\pm$ 1 standard deviation.

4 OMPS-LP aerosol extinction climatology

In order to study the aerosol extinction coefficient evolution after a volcanic eruption, the OMPS V1.0.9 product has to be averaged in some fashion. We have created two level 3 products, which are monthly and 10-day averaged Ext_{869}. Both products were put onto a regular grid with 2.5° latitude and 5° longitude steps.

An example of zonal monthly mean Ext_{869} averaged in 30° latitude bins for the whole OMPS operation period is presented in Fig. 2. In this figure, the volcanic eruptions and a relevant biomass burning event are shown with grey triangles with numbers. The information on the volcanic eruptions is presented in Tab. 1. We show only Ext_{869} within 60° in both hemispheres because, as it was pointed out in Sec. 3, the aerosol extinctions above these latitudes are associated with larger uncertainties.
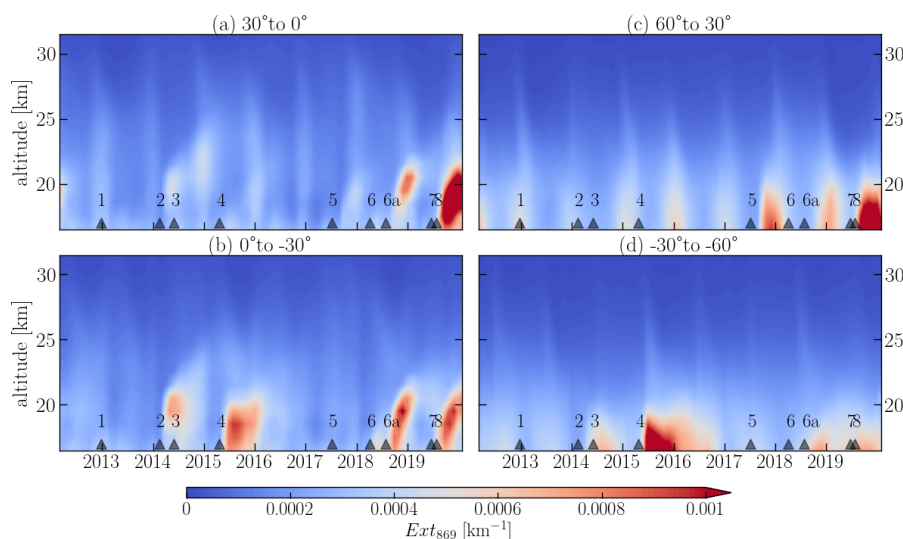
Figure 2. Monthly mean aerosol extinction coefficient (Ext_{869}) distribution with time and altitude. Ext_{869} was retrieved from OMPS-LP measurements and averaged over longitude in 30° latitude bins. The triangles with numbers represent volcanic eruptions and biomass burning events (see Tab. 1).

Table 1. Volcanic eruptions and biomass burning events shown in Fig. 2.

Number	Volcano	Date of the eruption	Latitude	Longitude
1	Copahue	23 Dec. 2012	-37.51	-71.1
2	Kelut	13 Feb. 2014	-7.55	112
3	Sangeang Api	30 May 2014	-8.2	119.07
4	Calbuco	22 Apr. 2015	-41.19	-72.37
5	Canadian Wildfires	July-Aug. 2017	51.64	-121.3
6	Ambae	06 Apr. 2018	-15.4	167.84
6a		27 July 2018		
7	Raikoke	22 June 2019	48.3	153.4
8	Ulawun	26 July 2019	-5.05	151.33

Furthermore, the main scope of this paper is to study the tropical Ambae eruptions; thus, we do not focus our attention on aerosol loading in the high latitudes.

Analysis of Fig. 2 shows that there is a certain increase of Ext_{869} in the very beginning of OMPS operation in the Northern Hemisphere latitude bins. This is associated with the eruption of Nabro (13° N) in the middle of 2011. Additionally, one can see an increase of Ext_{869} some time after eruptions from Table 1 and from Canadian Wildfires of 2017 (number 5 in Fig. 2 and Table 1). The degree of the enhancement, as well as the time lag between the eruptions, seen in the latitude bands, are

dependent on the volcano's location and the eruption strength. Usually, for the tropical eruptions, an increase in stratospheric
200 aerosol loading is seen globally because the aerosols and precursors are transported with the Brewer-Dobson Circulation (BDC)
to both hemispheres. Also, in the tropics, the BDC is responsible for the tape recorder effect, or delayed increase in Ext_{869}
with the height. For example, in Fig. 2 (a) and (b), the tape recorder effect is seen for the Kelut, Sangeang Api, Calbuco and
Ambae eruptions as well as for the Canadian Wildfires. For the eruptions in the mid-latitudes, the increase usually stays in the
hemisphere where it occurred (e.g., Oman et al., 2006; von Savigny et al., 2015; Toohey et al., 2019; Malinina, 2019).

205 Another noticeable feature in Fig. 2 is the periodical increase of Ext in all latitude bins. There are several factors causing
this pattern. For the tropical region, there is a periodic associated with the quasi-biennial oscillation (QBO). The influence of
QBO on stratospheric aerosols was previously reported by e.g. Hommel et al. (2015); Brinkhoff et al. (2015); von Savigny
et al. (2015); Malinina et al. (2018). Additionally, the annual seasonality in both tropics and mid-latitudes is related to two
factors. First, there are some yearly changes in stratospheric aerosol loading (Hitchman et al., 1994; Bingen et al., 2004). But
210 for the limb viewing instruments, the more important factor is the seasonality in solar scattering angle, which leads to artifacts
of the retrieval predominately in the extratropical regions (see e.g. Rieger et al., 2018).

5   Aerosol extinction coefficient evolution after Ambae eruption as seen by OMPS-LP

As it was already highlighted in the introduction, Ambae was one of the largest eruptions of the last decade but has not been
a focus of scientific or public interest. The eruptive period, which lasted over a year, had two explosive phases when SO_2 was
215 injected into the stratosphere (the exact information on SO_2 mass estimation can be found in Sec. 6.1). The first emission was
smaller, and the perturbation in Ext_{869} did not reach the altitudes above 21 km (see Fig. 2 (a) and (b)). The second emission
was considerably larger; it perturbed Ext_{869} up to 23.5 km in the tropics and up to 22 km in the extratropical regions. Although,
to better evaluate the plume evolution, we will further analyze 10-day averaged Ext_{869}.

The evolution with time and altitude of 10-day mean Ext_{869} averaged over longitudes at 18.5 and 20.5 km is presented in
220 panels (a) and (b) of Fig. 3. Foremost, it should be noted that the increase of Ext_{869} in February – May 2018 in the latitudes
above 25°N at 18.5 km and above 7°N at 20.5 km is related to the disappearing plume from the Canadian Wildfires of 2017.
The first small increase in Ext_{869} associated with the April Ambae eruption appears at 18.5 km in the first week after the
injection. The more significant increase is observed in early May 2018. At the time, the plume is located around 10–25°S
and stays there until late June. In June, the increase in Ext_{869} starts to spread to the south, reaching 35–45°S in July 2018.
225 At 20.5 km, the increase after the first SO_2 release is rather negligible. Nevertheless, there is still an area with the increased
aerosol loading below 20°S from the beginning of May.

In late July 2018, at the fourth phase of the eruption, Ambae injected another portion of ash and SO_2. Almost at the
same time, Ext_{869} increases at 18.5 km directly at the source. In about two weeks, the volcanic plume starts to spread both
northwards and southwards and is located between the equator and 35°S in early September, reaching 45°N in November –
230 December 2018. The southern border of the plume at 18 km is harder to identify because it mixes with the aerosol from the
previous SO_2 release. However, an increased aerosol loading is observed to the south of 35°S in September and intensifies
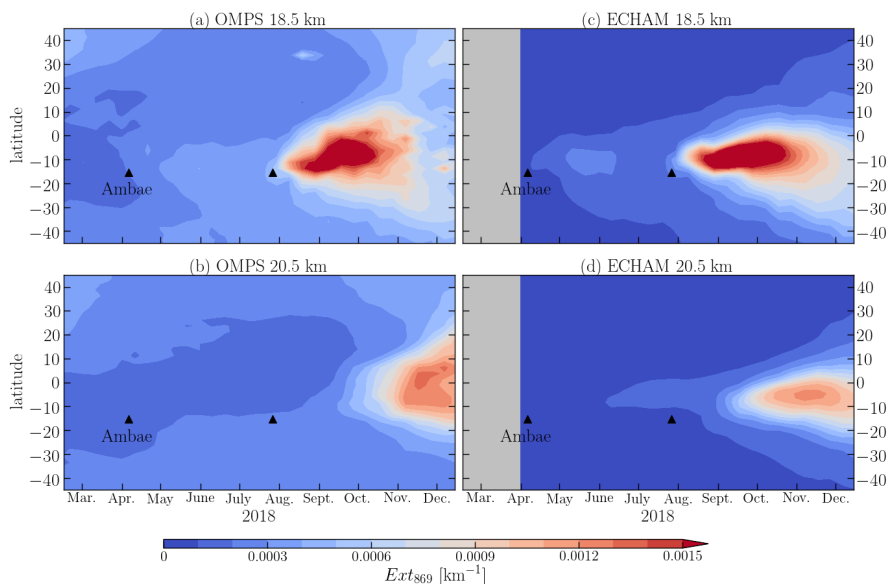
Figure 3. Evolution of the aerosol extinction coefficient (Ext_{869}) at 18.5 and 20.5 km altitude after Ambae eruptions of 2018. In panels (a) and (b) Ext_{869} was retrieved from OMPS-LP measurements; for panels (c) and (d) Ext_{869} was modelled by ECHAM-HAM. Both datasets were averaged over 10 day period.

further with the time. By mid October 2018, the plume starts to vanish around the equator and continues to weaken with time. At 20.5 km, the plume appears in mid-September 2018 at around 10°S, spreads northwards and southwards from that moment on, reaching its maximum in November. It is located in between 30° S and 35° N in mid December 2018. Again, at the southern border of the plume, there is an area of increased Ext_{869}, which is related to both eruptions.

6 Ambae eruption modelled with ECHAM-HAM

6.1 Estimation of SO$_2$ injection

In order to simulate the Ambae eruptions, as a first step the amount of SO$_2$ emissions and injection altitude should be determined. Although there are methods to retrieve SO$_2$ mass and altitude from nadir measurements, it is well known these methods do not allow to distinguish, if SO$_2$ was released into the stratosphere or into the upper troposphere (see e.g. Carboni et al., 2016). Carboni et al. (2016) suggest that the combination of limb and nadir instruments might give a better answer. For this reason, in our work we use a combination of MLS (Microwave Limb Sounder) (Pumphrey et al., 2015) and nadir SO$_2$ products to determine the altitude and the mass of SO$_2$ injection.

To assess the Ambae SO$_2$ burden and plume location, combined OMI (Ozone Monitoring Instrument) (Fioletov et al., 2011) and OMPS-NM (Carn et al., 2015) data were used for the April eruption. Yet for the July eruption, data from TROPOMI (TROPOspheric Monitoring Instrument) was taken into consideration. We do not use the same SO$_2$ satellite product for both

eruptive episodes because of two reasons. First, the TROPOMI data with a fine grid and extensive coverage is publicly available from the early May 2018, thus missing the first eruption. Second, even though the combined OMI and OMPS-NM dataset temporally covers both eruption phases, it contains spatial gaps, which results in less precise SO_2 mass assessment. Thus, the
250 current choice provides a trade-off between the spatial coverage and overall data availability.

For the injection altitude estimation, MLS SO_2 number density profiles and tropopause altitude were used. Using the plume location from OMI/OMPS-NM and TROPOMI data (see below), the profiles collocated with the plumes for April and July 2018 were analyzed. Based on that data, it was identified that on the 6 April and the 27 July, the volcanic SO_2 reached the stratosphere. These days coincide with the information presented by Moussallam et al. (2019); Kloss et al. (2020); Smithsonian
255 Institution (2019).

6.1.1 Combined OMI and OMPS-NM dataset

For the first eruption, OMI SO_2 level 2 data with the assumption of an SO_2 distribution in the lower stratosphere (center of mass altitude of 18 km (Li et al., 2017)) was used. Due to the OMI row anomaly, all rows > 21 (counting starts at 0) were excluded. The first ten rows were discarded in order to limit the across-track pixel width (Lu et al., 2013), so that only rows
260 10-21 were considered. Furthermore, the radiative cloud fractions less than 0.2 and a solar zenith angle less than 70° were required. SO_2 total columns with large negative values below -1E30 DU were not included in the analysis. A threshold of 0.05 g/m^2 was introduced to distinguish the volcanic signal from the background. All satellite pixels that fulfilled the above requirements were averaged for each segment of the self-defined grid (see below). The SO_2 data was converted into units of g/m^2 and multiplied with the segment area to obtain the SO_2 mass in units of g for every grid segment. All orbits measured on
265 one day were combined so that the SO_2 mass in each segment for a specific day was determined.

OMPS-NM level 2 SO_2 data with the SO_2 column for the lower stratosphere (16 km) was used accordingly. Pixels at the edges of the swath were discarded, excluding rows < 2 and rows > 33 (counting starts at 0) (Fioletov et al., 2020; Zhang et al., 2017). Only data with a pixel quality flag equal to 0 and a solar zenith angle less than 84° were used. Again, a threshold of 0.05 g/m^2 was applied, and the SO_2 mass per day for each grid segment was determined as described above for the OMI data.
270 The daily OMI and OMPS data were projected on a self-defined grid from 10° N to 45° S and from 150° E to 140° W with a resolution of 0.5° and averaged for each segment. The data was summed up over the entire grid to determine the total SO_2 mass for each day in this area. The results for the period from the beginning of March until the end of April 2018 are presented in the panel (a) of Fig. 4. The estimate for the day when SO_2 reached the stratosphere is marked with a red circle. Due to the large data gaps, this SO_2 mass is a minimum estimate for the SO_2 ejected during the eruption.
275 Before the 0.05 g/m^2 threshold was applied, the combined satellite measurements covered approximately 40–70% of the self-defined grid.

The largest source of error for estimating the SO_2 emission is probably the choice of the assumed SO_2 profile because the vertical distribution of the SO_2 affects the air mass factor used for the retrieval of the vertical column densities.
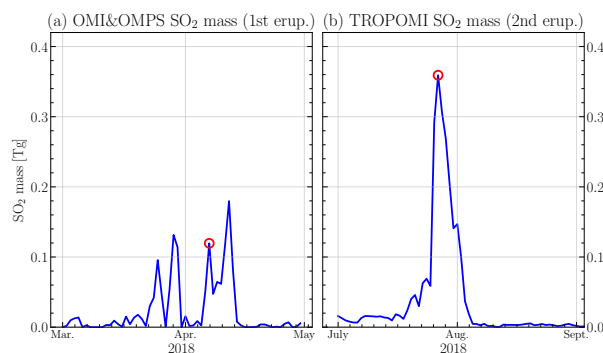
Figure 4. The SO_2 mass calculated for a threshold of 0.05 g/m^2 from the combined OMI and OMPS-NM for the first Ambae eruption in April (a) and from TROPOMI data for the July eruption (b).

6.2 TROPOMI dataset

280   The SO_2 mass emitted during the eruption of Ambae in late July of 2018 was estimated by analyzing SO_2 total vertical columns from the TROPOMI instrument (Veefkind et al., 2012) on the Copernicus Sentinel-5 Precursor satellite for the time period from the 1 July 2018 to the 29 September 2018. This instrument allows for global daily coverage of SO_2 with a spatial resolution of 3.5×7 km.

A grid with a resolution of $0.1°$ in longitude and latitude, respectively, was defined from $10°$ N to $45°$ S and $150°$ E to $140°$ W.
285   The utilized sulfur dioxide total vertical columns assuming an SO_2 profile represented by 1 km thick box filled with SO_2 and centered at 15 km altitude, in order to model conditions in an explosive eruption (Theys et al., 2017). Only vertical column densities with values less than 1000 mol/m^2 and a quality value greater than 0.5 were considered for the analysis (Pedergnana et al., 2018). The total vertical column was multiplied by the SO_2 molar mass to get the SO_2 mass loading in the units of g/m^2. Afterwards, a threshold of 0.05 g/m^2 was applied. The SO_2 mass loadings exceeding the selected threshold were averaged
290   in each grid segment, and the result multiplied by the segment area in order to obtain the SO_2 mass in units of g for every grid segment. Since some orbits overlap, 14 consecutive orbits covering a time span of approximately 24 h were bundled to a dataset batch and averaged for each grid segment. Finally, the SO_2 mass of the entire grid per batch are summed up to obtain the total SO_2 burden.

The SO_2 masses calculated for every batch and for the thresholds of 0.05 g/m^2 during the Ambae eruption are presented in
295   the panel (b) in Fig. 4. The date represents the date of the first orbit in each batch that intersects with the area of interest. With the red circle, the day SO_2 reached the stratosphere according to MLS data is marked. The SO_2 mass increased to a maximum of 0.36 ± 0.04 Tg on the 27 July and declined by the 5 August to magnitudes of Gg. The SO_2 mass for a threshold of 0 g/m^2 (not shown) exhibits a high SO_2 background of 0.2 Tg that is strongly increasing to a maximum of 0.57 Tg on the 27 July. It decreases to 0.15 Tg on the 5 August, before it goes back up to 0.27 Tg on the 14 August and decreases steadily afterwards.
300   The application of a threshold of 0 g/m^2 seems to suggest an SO_2 background of approximately 0.2 Tg that is not apparent in

Fig. 4, using a more restrictive threshold. Focusing only on the additional SO_2 entry, i.e. the difference between the maximum SO_2 and the background emission of 0.2 Tg, a total burden of approximately 0.4 Tg SO_2 was emitted applying a threshold of $0\,\mathrm{g/m^2}$. This result is comparable to the maximal SO_2 burden in Fig. 4.

Furthermore, the calculated maximum of emitted SO_2 mass strongly depends on the SO_2 data product used. As mentioned
305 in Sec. 6.1.1, the vertical SO_2 distribution affects the air mass factor that is used to retrieve the vertical column densities. Assuming a threshold of $0.05\,\mathrm{g/m^2}2$ and an SO_2 profile with the SO_2 existing in a 1 km thick box at an altitude of 15 km, as discussed above, results in the maximal SO_2 mass of 0.36 Tg. This value increases to 0.57 Tg and even to approximately 1.6 Tg by assuming a 7 km profile and a profile from the TM5 model, respectively, emphasizing the importance of a reasonable assumption for the vertical SO_2 distribution.

6.3   Model experiment

310

The volcanic eruptions were modeled by MAECHAM5-HAM. ECHAM is a general circulation model (GCM) which was used in the middle atmosphere version of the GCM ECHAM5 (Giorgetta et al., 2006). The horizontal resolution was about $1.8°$, spectral truncation at wave-number 63 (T63) with 95 vertical layers up to $0.01\,\mathrm{hPa}$. The large wave numbers of the model were nudged to ERA5 reanalysis data (Hersbach et al., 2018) to achieve realistic wind and transport conditions.

315   Interactively coupled to ECHAM is the aerosol microphysical model HAM (Stier et al., 2005), which calculates the oxidation of sulfur and sulfate aerosol formation, including nucleation, accumulation, condensation and coagulation processes. A simple stratospheric sulfur chemistry is applied above the tropopause (Timmreck, 2001; Hommel et al., 2011). The sulfate is radiatively active for both SW and LW radiation and coupled to the radiation scheme of ECHAM. These simulations use the model setup described in Niemeier et al. (2009) and Niemeier and Timmreck (2015). Hereafter we refer to MECHAM5-HAM as ECHAM.

320   The experiment setup used the estimated SO_2 emissions from Sec. 6.1. We injected 0.12 Tg SO_2 at altitudes of 82 to $102\,\mathrm{hPa}$ on the 6 April for four hours and 0.36 Tg SO_2 at altitudes between 74 and $90\,\mathrm{hPa}$ on the 27 July for 24 hours, starting at 18h UTC. The long eruption phase was chosen to take the observed series of eruptions into account. To slow down the oxidation of SO_2 due to the limited availability of OH in a volcanic cloud (Mills et al., 2017), the concentration of OH was limited in the first days after the eruption: Day 1 to 10 to 40% and day 10 to 20 to 60% of the prescribed OH. The sea surface temperature
325   (SST) is set to a climatological value (Hurrell et al., 2008).

In order to be consistent with OMPS-LP measurements, the output of ECHAM was interpolated to the same altitudinal grid as provided by OMPS-LP. ECHAM provides Ext at 550 and 825 nm, thus, for the comparison consistency, the simulated Ext was recalculated to 869 nm and afterwards the 10-day averages were calculated.

6.4   Aerosol extinction coefficient evolution after Ambae eruption as modelled by ECHAM

330   The simulated distribution of Ext_{869} with time and latitude at 18.5 and 20.5 km is presented in panels (c) and (d) of Fig. 3. In these panels, it is seen that at 18.5 km the aerosol extinction coefficient starts to increase almost right after the first eruption and reaches its peak in May. The main part of the volcanic aerosol stays in the tropics between 30° S and the equator. A small amount of aerosol is dispersed meridionally right after the eruption. After the second eruption, at the end of July, the

first aerosol is formed right after the eruption with Ext increasing slowly until it reaches the maximum in September. Most

335 aerosol is located to the south of 10° N. In the last days of September, the plume is still very well pronounced and it starts to spread meridionally, mostly southwards. By beginning of October Ext increases also in the Northern Hemisphere at 20° N, this increase spreads with the time to 40° in the late December. The plume starts to weaken in the beginning of November.

At 20.5 km the plume from the first eruption appears in late June. The plume at this altitude is quite weak and does not extend much over the latitudes. Basically, it is a small blob in between the equator and 10° S. The increase in Ext associated

340 with the second eruption appears at 20.5 km in very late August, by the middle of September the plume intensifies and starts to expand meridionally. It reaches its maximum by November, when the increase is seen from 10° N to 40° S. From that moment, the plume starts to slowly disappear. In late December, the Ext increase is seen from 30° N to 45° S.

7 Discussion

7.1 Aerosol extinction coefficient

345 In order to evaluate the consistency of the results from OMPS and ECHAM, panels (a), (b) and (c), (d) of Fig. 3 need to be compared. It is obvious that the model and the observations are very close to each other, in particular, at 18.5 km. The plume from the first eruption appears and intensifies at the same time at 18.5 km; however, in the model, it is weaker, and it reaches 20.5 km about a month later. This is most likely related to the fact that in the model, neither the anthropogenic nor biomass burning sources are taken into account.

350 The Ambae plume from the July eruption looks even more similar in the model results and measurements. Not only the plume appears at the same time at 18.5 km and is located at the same latitudes, but also both model and measurements show a wave-shape of the plume. The curvature in both plumes appears in mid September, however, in the OMPS-LP data, the plume is bending stronger to the north. It should also be noted that the ECHAM simulations show a more intensive and longer living plume at this altitude. Additionally, in the OMPS-LP data, in the second part of October, the aerosols move evenly north-

355 and southward, while in the ECHAM data, the plume is transported rather to the south. In ECHAM data at 20.5 km, the July plume appears about two-three weeks earlier than in the OMPS measurements. Though the intensity of the modeled plume at this altitude is slightly weaker, the absolute differences are smaller than at 18.5 km. However, the horizontal distribution of the modeled plume is less consistent with the measurements. While the plume in ECHAM stays with the time at the same geographical location mostly in the Southern hemisphere, in the OMPS data, it has a C-shape around the equator.

360 It should be highlighted that even though there are some differences between the modeled and measured Ext, the consistency is quite remarkable. There are two main factors which contributed to this particular agreement between OMPS and ECHAM, namely, rather precise SO_2 mass and height estimation as well as nudging of meteorological data. Thus, it is seen that the second plume, whose emission was estimated from TROPOMI data, was modeled more accurately. At the same time, our internal studies showed that the ECHAM SO_2 sensitivity plays a key role in the lifetime and distribution of the plume.

365 It is a well-known feature of ECHAM that the meridional transport is too strong, causing a relatively short lifetime of sulfate (e.g. Niemeier et al., 2009), especially compared to results of other models (e.g. Marshall et al., 2018). Therefore, the nudging
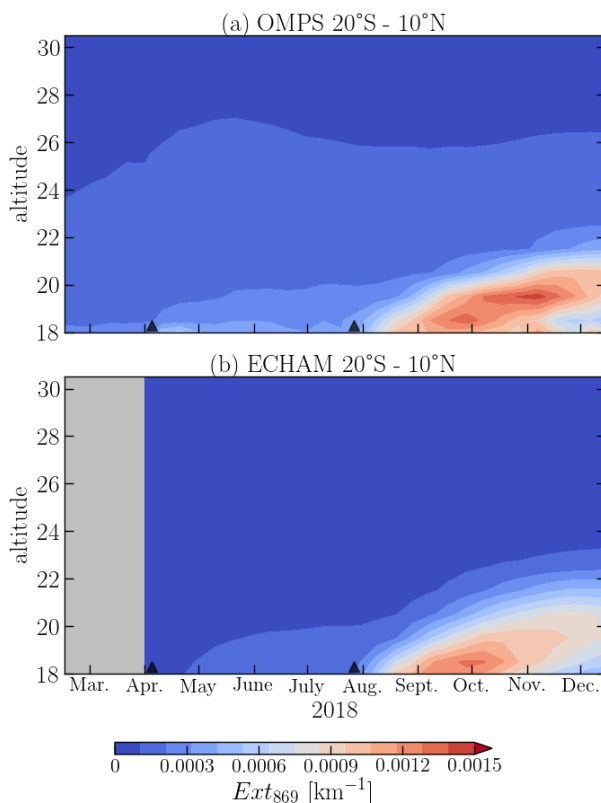
Figure 5. Evolution of zonal mean aerosol extinction coefficient (Ext_{869}) in the tropics ($20°S - 20°N$) with altitude and time after Ambae eruptions of 2018. In the panel (a) the data from OMPS-LP is presented, in the panel (b) the simulation with ECHAM is plotted. Both datasets were averaged over a 10-day period.

of the meteorological data provided a realistic transport pattern resulting in good agreement with OMPS-LP measurements. However, the nudging database, the ERA5 reanalysis, is a model product as well. Thus, small differences to observations are rather possible, especially in the stratosphere. Additionally, the stratospheric aerosol layer is close to the ozone layer at 24 km.

370   ECHAM uses prescribed ozone and OH values, which do not change due to the presence of volcanic aerosol.

Another way to assess the degree of consistency between the model and the measurements is to analyze the vertical distribution of Ext with the time (see Fig. 5). Since most of the plume stayed in the tropical region, for Fig. 5 the OMPS (panel (a)) and ECHAM (panel (b)) Ext were averaged between 20° S and 10° N. In this figure, it is again obvious that in the model the perturbation from the volcano reached the same altitudes. Additionally, it is seen that the plume was weaker for the April

375   eruption. However, consistency for the second eruption is again striking. Not only the plume has the same overall shape, but it is located at the same time coordinates, with the only exception of a slightly increased blob in the OMPS data at 19.5 km in November. Thus, vertical transport is slightly weaker in ECHAM, which explains some of the differences to the OMPS data in the horizontal cross-section at 20.5 km.

Here it should be highlighted again that the vertical lofting of the volcanic cloud is related to the BDC with an upward
branch in the tropics. The patterns in Fig. 5 are a prime example of the stratospheric tape-recorder effect, noticed earlier. For
the model experiment, one should bear in mind that the absorption of terrestrial radiation by stratospheric aerosols causes an
additional vertical updraft which enhances the BDC effect in the tropics (Niemeier et al., 2011).

7.2 Radiative forcing

In order to assess the RF from Ambae eruption, we analyzed the ECHAM RF output as well as the RF calculated from OMPS-
LP measurements. For the latter, we use the empirical approximation given by Eq. (1) as suggested by Hansen et al. (2005):

$$RF \approx -25 \cdot \tau_{550}, \tag{1}$$

where τ_{550} is the stratospheric aerosol optical depth at 550 nm. Although originally proposed for the globally averaged model
data, Eq. (1) was used for the RF assessment from the measurement results as well (see e.g. Solomon et al., 2011; von Savigny
et al., 2015). As the focus of our study is on the additional RF after the tropical Ambae eruptions, we do not consider global
averages but limit the comparison to 20° S – 20°N region.

To apply Eq. (1) to the OMPS-LP data, we determined $\tau_{550(869)}$ by integrating the Ext_{869} from instantaneous tropopause
height to 33.5 km and then converted the result to 550 nm wavelength by using an Ångström exponent of 2.47, which is
appropriate for the particle size distribution used in the Ext_{869} retrieval (see Sec. 2). The tropopause height values were
obtained for each single OMPS-LP measurement by using corresponding ECMWF-ERA5 temperature profiles. The WMO
definition of the tropopause based on the temperature lapse rate was implemented (WMO, 1957). Afterwards the $\tau_{550(869)}$
values were averaged over 10-days period. For consistency, we also applied Eq. (1) to the ECHAM τ. Additionally, from
all datasets mean tropical τ in the period from 01 April to 19 July 2018 was subtracted to remove the effects of background
aerosol. Even though the chosen period contains the effects of the first weaker Ambae eruption, it is a common "cleaner" period
available for all datasets and thus is considered to be optimal for the study.

The normalized RFs are presented in Fig. 6. Here, the tropical all-sky RF, calculated as an anomaly to a control simulation
without the Ambae eruption, is presented with a green line as a function of time. The OMPS-LP RF, calculated employing
Eq. (1), is shown with a red line. To illustrate the validity of the Hansen's formula to a non-global dataset, it was also applied to
the τ_{550} obtained directly from the ECHAM model. The result is shown with the solid blue line in the figure. The influence of
the assumed particle size distribution on the Ext and/or τ conversion to a different wavelength is illustrated by the recalculation
of ECHAM τ_{869} to $\tau_{550(869)}$ using the fixed Ångström exponent as it was done for OMPS-LP. The RF resulting from Eq. (1)
applied to ECHAM τ_{869} converted to $\tau_{550(869)}$ is presented with a dashed blue line in Fig. 6. Both dates of Ambae eruptions
are marked with vertical dotted grey lines.

Analyzing the Fig. 6, it becomes obvious that the effect of the first smaller Ambae eruption is negligible for the RF. All four
lines show almost no temporal change in between the eruptions (1 April to 27 July 2018) and are located around 0 W/m².
Even though from all datasets the RF for the period was subtracted, it was a mean value, resulting in temporal behavior being
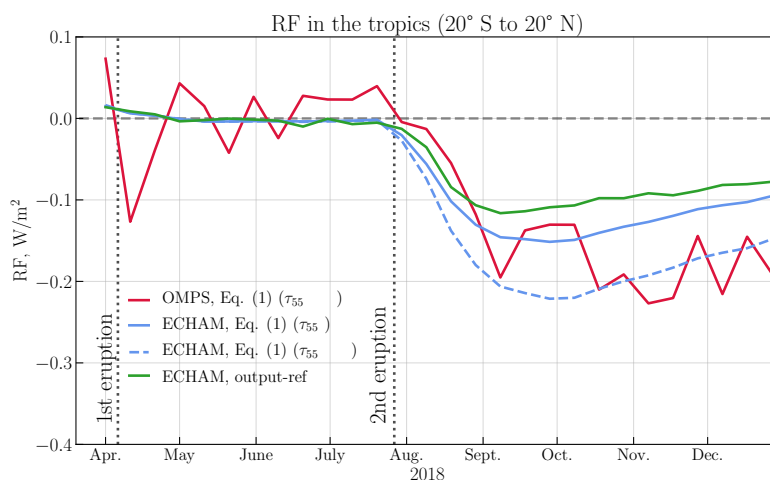
Figure 6. The radiative forcing (RF) from ECHAM and OMPS-LP averaged over the tropics (20° S – 20° N). The green line shows the difference between ECHAM internal RF calculated accounting for and neglecting the Ambae eruptions. Red and blue lines show respectively the RF calculated with Eq. (1) from OMPS-LP τ_{869} converted to $\tau_{550(869)}$, ECHAM τ_{550} (blue solid) and ECHAM τ_{869} converted to $\tau_{550(869)}$ (blue dashed). From all datasets the respective mean RF in the period from the 1 April to the 19 July 2018 was subtracted.

unaffected by this normalization. After the second eruption, all four lines drop significantly. The ECHAM internal RF (green line) reaches its maximum of -0.11 W/m^2 in the first week of September, and afterwards the RF declines slowly up to -0.08 W/m^2 by the late December 2018. The solid blue line, or the RF calculated with Eq. (1) from ECHAM τ_{550}, has very

415   similar behavior with the green line; however, it reaches the maximum (-0.13 W/m^2) in the late September and keeps the offset from the green line by ≈0.02 W/m^2 until the end of 2018. The calculated RF from ECHAM $\tau_{550(869)}$ reaches its maximum at the same time as the solid blue line, but its absolute value is significantly larger (-0.22 W/m^2). Further with time, the offset between dashed and solid blue lines becomes somewhat smaller, reaching a value of 0.05 W/m^2 in December. At the same time, the red line showing the RF calculated with Eq. 1 from OMPS-LP drops heavily after the second eruption but becomes

420   noisier from September on. The maximum in RF (-0.22 W/m^2) is observed in November 2018, which agrees with panel (a) of Fig. 5. The OMPS-LP RF decreases afterwards to about -0.19 W/m^2 by the end of the year.

     In the discussion of Fig. 6, it is important to draw reader's attention to the offset between the ECHAM RFs calculated with Eq. (1) from τ_{550} and $\tau_{550(869)}$. After the second eruption, the difference reaches up to 70%. This difference is a prime example of the influence of assumed particle size distribution parameters on the RF calculations. For example, at the plume maximum,

425   the difference is almost as large as the forcing, but it decreases while the stratosphere relaxes. Considering these discrepancies, the respective similarities of the ECHAM $\tau_{550(869)}$ and OMPS-LP RFs (dashed blue and red lines), as well as ECHAM τ_{550} and ECHAM output (solid blue and green lines), are remarkable. Here it should be noted that although there are obvious differences between the curves, they generally have quite good temporal correlation and capture the second eruption very well.

Combining the above mentioned facts, the following conclusion can be drawn. Even when applied to the tropical region
430   rather than globally, the Hansen's formula given by Eq. (1) provides a reliable approximation of RF with about 20% accuracy.
In turn, the τ conversion to a different wavelength is a more significant source of uncertainty with a potential to increase the
estimated RF by up to 70%. After accounting for those uncertainties, a very good agreement between the RF values from
ECHAM and those from OMPS-LP is observed. For the particular Ambae eruption studied in this paper, we estimate the
tropical radiative forcing caused by an increase in stratospheric aerosols to be about -0.13 $\mathrm{W/m^2}$.

435   **8   Conclusions**

The distribution of aerosol extinction coefficients at 869 nm in the stratosphere after the 2018 Ambae eruption was compared
using the data retrieved from the OMPS-LP observations and that modeled by ECHAM.

We present here the retrieval algorithm (V1.0.9) of stratospheric aerosol extinction coefficient profiles at 869 nm from the
OMPS-LP instrument. The retrieval algorithm was adopted from SCIAMACHY V1.4 and shows similar results in comparison
440   with solar occultation instruments. The comparison of OMPS V1.0.9 product with the aerosol extinction coefficient observa-
tions from SAGE III/ISS showed that the mean relative difference is less than 25% for the profiles in between 40° S and 40° N.
In the higher latitudes, the difference is somewhat larger; it is less than 35% below 25 km but can reach about 60% at 28 km.

We also show the changes in the aerosol extinction coefficient after the 2018 Ambae eruption using monthly mean and 10-
day average data. Ambae caused one of the largest perturbations in the aerosol layer for the OMPS operating period. Volcanic
445   aerosols rise over time to about 21 km in the tropics within the tropical pipe of BDC (the tape-recorder effect). Analysing
the 10-day average data, it has been seen that the plume from the first phase of the eruption was relatively weak and did not
spread outside tropics. The second eruption in July was much larger, and the aerosols also spread to the mid-latitudes of both
hemispheres.

The measurement data was compared with the model output from a global aerosol model (ECHAM). In order to simulate
450   the Ambae eruption accurately, the injected SO_2 emission was estimated using combined OMPS and OMI data for the April
eruption (0.12 Tg) and TROPOMI data for the July eruption (0.36 Tg). The altitudinal distribution of the SO_2 was assessed
using MLS profiles. Thus, the resulting simulation showed that the model and measurements agree well with each other. The
main differences concern the intensity and the lifetime of the volcanic perturbation. While for the first eruption, ECHAM
underestimated the strength of plume as well as the time it reached 20.5 km altitude; for the second eruption, the modeled
455   plume reached higher altitudes about two to three weeks earlier, and the plume lived longer, being overall slightly weaker at
that altitude. Although the differences in the measured and modeled plumes exist, they are rather minor, and the consistency
is remarkable. The good agreement is explained by the rather precise SO_2 injection mass and height assessment, as well as by
the nudging of meteorological data.

We also compare aerosol radiative forcing (RF) caused by the increase in stratospheric aerosol loading from the second
460   Ambae eruption in the tropics. While the time courses of RF for the ECHAM output and ECHAM and OMPS-LP recalculated
RFs generally agree quite well, the absolute values vary significantly. The empirical formula used in our assessment works

well not only for the globally averaged aerosol optical depths but also for the tropical region. However, this approach suffers from the errors associated with the assumed particle size distribution for the datasets where the Ångtsröm exponent has to be used. We estimate the RF in the tropics after the second 2018 Ambae eruption to be about -0.13 $\mathrm{W/m}^2$.

465   In general, if the initial data (SO_2 mass, day and height of injection as well as meteorological data) is quite precise, the models give a very good estimate of the plume distribution, and the calculation of the radiative forcing can be made for an isolated plume without additional assumptions. Overall, the best results can be achieved only by combining observational data and modeling capabilities. Thus, it is very important to unite the measurement and model community together, for example, as the research unit VolImpact does (von Savigny et al., 2020).

470   *Code and data availability.* OMPS-LP aerosol extinction coefficient at 869 nm data are available after registration at http://www.iup.uni-bremen.de/DataRequest/. ECHAM primary data and scripts used in the analysis and other supplementary information that may be useful in reproducing the authors model work are archived by the Max Planck Institute for Meteorology and can be obtained by contacting publications@mpimet.mpg.de. Model results will be available under cera-www.dkrz.de soon.

Author contributions. EM initiated the study, provided OMPS-LP aerosol extinction coefficient product, compared it to SAGE-III/ISS,
475   prepared the Figures and wrote most of the paper text (Sec. 1 - 5, 6.4, 7 and 8). AR developed the retrieval software, supervised the work at the University of Bremen and revised the paper. UN performed model simulations, wrote Sec. 6.3 and 7, helped with the literature survey and revised the text. SP performed SO_2 mass estimations, wrote Sec. 6.1 and revised the text. CA formatted OMPS L1 data, analyzed MLS data, provided tropopause heights for OMPS-LP and revised the text. FW actively participated in the result discussions and revised the text. CT helped with literature survey; CvS and CT initiated and proposed the research unit, they and JPB led the project and revised the text.

480   *Competing interests.* The authors declare no competing interests.

Acknowledgements. This work was funded in parts by the German Research Foundation (DFG) through the research unit VolImpact (FOR 2820): projects VolARC, VolDyn and VolClim, ESA through Ozone-CCI+ project, and the University of Bremen and state of Bremen. The model simulations were performed on the computer of the Deutsches Klima Rechenzentrum (DKRZ). We are also thankful to NASA for OMI (NASA GES DISC, 2020a) and OMPS-NM (NASA GES DISC, 2020b) L2 data as well as for OMPS-LP L1 data which was downloaded
485   from the NASA Langley Research Center EOSDIS Distributed Active Archive Center. MLS and SAGE-III/ISS L2 data was obtained from NASA's Earthdata (2020a) and NASA's Earthdata (2020b) respectively. S5P TROPOMI data was downloaded from S5P Data Hub (2020).

References

Arosio, C., Rozanov, A., Malinina, E., Eichmann, K.-U., von Clarmann, T., and Burrows, J. P.: Retrieval of ozone profiles from OMPS limb scattering observations, Atmospheric Measurement Techniques, 11, 2135–2149, https://doi.org/10.5194/amt-11-2135-2018, https://www.atmos-meas-tech.net/11/2135/2018/, 2018.

Bertaux, J., Hauchecorne, A., Dalaudier, F., Cot, C., Kyrölä, E., Fussen, D., Tamminen, J., Leppelmeier, G., Sofieva, V., Hassinen, S., et al.: First results on GOMOS/Envisat, Advances in Space Research, 33, 1029–1035, 2004.

Bingen, C., Fussen, D., and Vanhellemont, F.: A global climatology of stratospheric aerosol size distribution parameters derived from SAGE II data over the period 1984–2000: 1. Methodology and climatological observations, Journal of Geophysical Research: Atmospheres, 109, 2004.

Bourassa, A. E., Rieger, L. A., Zawada, D. J., Khaykin, S., Thomason, L., and Degenstein, D. A.: Satellite Limb Observations of Unprecedented Forest Fire Aerosol in the Stratosphere, Journal of Geophysical Research: Atmospheres, https://doi.org/10.1029/2019JD030607, 2019.

Brinkhoff, L. A., Rozanov, A., Hommel, R., von Savigny, C., Ernst, F., Bovensmann, H., and Burrows, J. P.: Ten-Year SCIAMACHY Stratospheric Aerosol Data Record: Signature of the Secondary Meridional Circulation Associated with the Quasi-Biennial Oscillation, in: Towards an Interdisciplinary Approach in Earth System Science, pp. 49–58, Springer, 2015.

Brühl, C., Schallock, J., Klingmüller, K., Robert, C., Bingen, C., Clarisse, L., Heckel, A., North, P., and Rieger, L.: Stratospheric aerosol radiative forcing simulated by the chemistry climate model EMAC using Aerosol CCI satellite data, Atmospheric Chemistry and Physics, 18, 12 845–12 857, https://doi.org/10.5194/acp-18-12845-2018, https://www.atmos-chem-phys.net/18/12845/2018/, 2018.

Carboni, E., Grainger, R. G., Mather, T. A., Pyle, D. M., Thomas, G. E., Siddans, R., Smith, A. J. A., Dudhia, A., Koukouli, M. E., and Balis, D.: The vertical distribution of volcanic SO_2 plumes measured by IASI, Atmospheric Chemistry and Physics, 16, 4343–4367, https://doi.org/10.5194/acp-16-4343-2016, https://www.atmos-chem-phys.net/16/4343/2016/, 2016.

Carn, S., Yang, K., Prata, A., and Krotkov, N.: Extending the long-term record of volcanic SO2 emissions with the Ozone Mapping and Profiler Suite nadir mapper, Geophysical Research Letters, 42, 925–932, 2015.

Chen, Z., Bhartia, P. K., Loughman, R., Colarco, P., and DeLand, M.: Improvement of stratospheric aerosol extinction retrieval from OMPS/LP using a new aerosol model, Atmospheric Measurement Techniques, 11, 6495–6509, https://doi.org/10.5194/amt-11-6495-2018, https://www.atmos-meas-tech.net/11/6495/2018/, 2018.

Chen, Z., Bhartia, P. K., Torres, O., Jaross, G., Loughman, R., DeLand, M., Colarco, P., Damadeo, R., and Taha, G.: Evaluation of OMPS/LP Stratospheric Aerosol Extinction Product Using SAGE III/ISS Observations, Atmospheric Measurement Techniques Discussions, 2019, 1–27, https://doi.org/10.5194/amt-2019-360, https://www.atmos-meas-tech-discuss.net/amt-2019-360/, 2019.

Cisewski, M., Zawodny, J., Gasbarre, J., Eckman, R., Topiwala, N., Rodriguez-Alvarez, O., Cheek, D., and Hall, S.: The Stratospheric Aerosol and Gas Experiment (SAGE III) on the International Space Station (ISS) Mission, in: Sensors, Systems, and Next-Generation Satellites XVIII, vol. 9241, p. 924107, International Society for Optics and Photonics, 2014.

Damadeo, R., Zawodny, J., Thomason, L., and Iyer, N.: SAGE version 7.0 algorithm: application to SAGE II, Atmospheric Measurement Techniques, 6, 3539–3561, 2013.

Dhomse, S. S., Mann, G. W., Antuña Marrero, J. C., Shallcross, S. E., Chipperfield, M. P., Carslaw, K. S., Marshall, L., Abraham, N. L., and Johnson, C. E.: Evaluating the simulated radiative forcings, aerosol properties and stratospheric warmings from the 1963

Agung, 1982 El Chichón and 1991 Mt Pinatubo volcanic aerosol clouds, Atmospheric Chemistry and Physics Discussions, 2020, 1–45, https://doi.org/10.5194/acp-2020-344, https://www.atmos-chem-phys-discuss.net/acp-2020-344/, 2020.

525 Feinberg, A., Sukhodolov, T., Luo, B.-P., Rozanov, E., Winkel, L. H., Peter, T., and Stenke, A.: Improved tropospheric and stratospheric sulfur cycle in the aerosol-chemistry-climate model SOCOL-AERv2, Geoscientific Model Development, 12, 3863–3887, 2019.

Fioletov, V., McLinden, C., Krotkov, N., Moran, M., and Yang, K.: Estimation of SO2 emissions using OMI retrievals, Geophysical Research Letters, 38, 2011.

Fioletov, V., McLinden, C. A., Griffin, D., Theys, N., Loyola, D. G., Hedelt, P., Krotkov, N. A., and Li, C.: Anthropogenic and volcanic
530 point source SO_2 emissions derived from TROPOMI onboard Sentinel 5 Precursor: first results, Atmospheric Chemistry and Physics Discussions, 2020, 1–30, https://doi.org/10.5194/acp-2019-1095, https://www.atmos-chem-phys-discuss.net/acp-2019-1095/, 2020.

Fischer, H., Birk, M., Blom, C., Carli, B., Carlotti, M., Clarmann, T. v., Delbouille, L., Dudhia, A., Ehhalt, D., Endemann, M., et al.: MIPAS: an instrument for atmospheric and climate research, Atmospheric Chemistry and Physics, 8, 2151–2188, 2008.

Fussen, D. and Bingen, C.: Volcanism dependent model for the extinction profile of stratospheric aerosols in the UV-visible range, Geophys-
535 ical research letters, 26, 703–706, 1999.

Giorgetta, M. A., Manzini, E., Roeckner, E., Esch, M., and Bengtsson, L.: Climatology and forcing of the quasi–biennial oscillation in the MAECHAM5 model, J. Climate, 19, 3882–3901, 2006.

Gottwald, M. and Bovensmann, H.: SCIAMACHY - Exploring the Changing Earth's Atmosphere, Springer, Dordrecht, https://doi.org/10.1007/978-90-481-9896-2, 2011.

540 Hansen, J., Sato, M., Ruedy, R., Nazarenko, L., Lacis, A., Schmidt, G., Russell, G., Aleinov, I., Bauer, M., Bauer, S., et al.: Efficacy of climate forcings, Journal of Geophysical Research: Atmospheres, 110, 2005.

Haywood, J. M., Jones, A., Clarisse, L., Bourassa, A., Barnes, J., Telford, P., Bellouin, N., Boucher, O., Agnew, P., Clerbaux, C., et al.: Observations of the eruption of the Sarychev volcano and simulations using the HadGEM2 climate model, Journal of Geophysical Research: Atmospheres, 115, 2010.

545 Haywood, J. M., Jones, A., and Jones, G. S.: The impact of volcanic eruptions in the period 2000–2013 on global mean temperature trends evaluated in the HadGEM2-ES climate model, Atmospheric Science Letters, 15, 92–96, 2014.

Hersbach, H., de Rosnay, P., Bell, B., Schepers, D., Simmons, A., Soci, C., Abdalla, S., Alonso-Balmaseda, M., Balsamo, G., Bechtold, P., et al.: Operational global reanalysis: progress, future directions and synergies with NWP, ERA Report Series, ECMWF, Shinfield Park, 2018.

550 Hess, M., Koepke, P., and Schult, I.: Optical properties of aerosols and clouds: The software package OPAC, Bulletin of the American meteorological society, 79, 831–844, 1998.

Hitchman, M. H., McKay, M., and Trepte, C. R.: A climatology of stratospheric aerosol, Journal of Geophysical Research: Atmospheres, 99, 20 689–20 700, 1994.

Hommel, R., Timmreck, C., and Graf, H. F.: The global middle-atmosphere aerosol model MAECHAM5-SAM2: comparison with
555 satellite and in-situ observations, Geoscientific Model Development, 4, 809–834, https://doi.org/10.5194/gmd-4-809-2011, http://www.geosci-model-dev.net/4/809/2011/, 2011.

Hommel, R., Timmreck, C., Giorgetta, M. A., and Graf, H. F.: Quasi-biennial oscillation of the tropical stratospheric aerosol layer, Atmospheric Chemistry and Physics, 15, 5557–5584, https://doi.org/10.5194/acp-15-5557-2015, https://www.atmos-chem-phys.net/15/5557/2015/, 2015.

560 Hurrell, J. W., Hack, J. J., Shea, D., Caron, J. M., and Rosinski, J.: A New Sea Surface Temperature and Sea Ice Boundary Dataset for the Community Atmosphere Model, Journal of Climate, 21, 5145–5153, https://doi.org/10.1175/2008JCLI2292.1, https://doi.org/10.1175/2008JCLI2292.1, 2008.

Ivy, D. J., Solomon, S., Kinnison, D., Mills, M. J., Schmidt, A., and Neely, R. R.: The influence of the Calbuco eruption on the 2015 Antarctic ozone hole in a fully coupled chemistry-climate model, Geophysical Research Letters, 44, 2556–2561, 2017.

565 Jaross, G., Bhartia, P. K., Chen, G., Kowitt, M., Haken, M., Chen, Z., Xu, P., Warner, J., and Kelly, T.: OMPS Limb Profiler instrument performance assessment, Journal of Geophysical Research: Atmospheres, 119, 4399–4412, https://doi.org/10.1002/2013JD020482, http://dx.doi.org/10.1002/2013JD020482, 2014.

Khaykin, S., Godin-Beekmann, S., Hauchecorne, A., Pelon, J., Ravetta, F., and Keckhut, P.: Stratospheric smoke with unprecedentedly high backscatter observed by lidars above southern France, Geophysical Research Letters, 45, 1639–1646, 2018.

570 Kloss, C., Berthet, G., Sellitto, P., Ploeger, F., Bucci, S., Khaykin, S., Jégou, F., Taha, G., Thomason, L. W., Barret, B., Le Flochmoen, E., von Hobe, M., Bossolasco, A., Bègue, N., and Legras, B.: Transport of the 2017 Canadian wildfire plume to the tropics via the Asian monsoon circulation, Atmospheric Chemistry and Physics, 19, 13 547–13 567, https://doi.org/10.5194/acp-19-13547-2019, https://www.atmos-chem-phys.net/19/13547/2019/, 2019.

Kloss, C., Sellitto, P., Legras, B., Vernier, J.-P., Jégou, F., Venkat Ratnam, M., Kumar, B. S., Madhavan, B. L., and Berthet, G.: Impact 575 of the 2018 Ambae eruption on the global stratospheric aerosol layer and climate, Journal of Geophysical Research: Atmospheres, p. e2020JD032410, 2020.

Kravitz, B., Robock, A., and Bourassa, A.: Negligible climatic effects from the 2008 Okmok and Kasatochi volcanic eruptions, Journal of Geophysical Research: Atmospheres, 115, 2010.

Kravitz, B., Robock, A., Bourassa, A., Deshler, T., Wu, D., Mattis, I., Finger, F., Hoffmann, A., Ritter, C., Bitar, L., et al.: Simulation and 580 observations of stratospheric aerosols from the 2009 Sarychev volcanic eruption, Journal of Geophysical Research: Atmospheres, 116, 2011.

Kremser, S., Thomason, L. W., Hobe, M., Hermann, M., Deshler, T., Timmreck, C., Toohey, M., Stenke, A., Schwarz, J. P., Weigel, R., et al.: Stratospheric aerosol—Observations, processes, and impact on climate, Reviews of Geophysics, 2016.

Li, C., Krotkov, N. A., Carn, S., Zhang, Y., Spurr, R. J. D., and Joiner, J.: New-generation NASA Aura Ozone Monitoring Instrument (OMI) 585 volcanic SO₂ dataset: algorithm description, initial results, and continuation with the Suomi-NPP Ozone Mapping and Profiler Suite (OMPS), Atmospheric Measurement Techniques, 10, 445–458, https://doi.org/10.5194/amt-10-445-2017, https://www.atmos-meas-tech.net/10/445/2017/, 2017.

Llewellyn, E., Lloyd, N., Degenstein, D., Gattinger, R., Petelina, S., Bourassa, A., Wiensz, J., Ivanov, E., McDade, I., Solheim, B., et al.: The OSIRIS instrument on the Odin spacecraft, Canadian Journal of Physics, 82, 411–422, 2004.

590 Loughman, R., Bhartia, P. K., Chen, Z., Xu, P., Nyaku, E., and Taha, G.: The Ozone Mapping and Profiler Suite (OMPS) Limb Profiler (LP) Version 1 aerosol extinction retrieval algorithm: theoretical basis, Atmospheric Measurement Techniques, 11, 2633–2651, https://doi.org/10.5194/amt-11-2633-2018, https://www.atmos-meas-tech.net/11/2633/2018/, 2018.

Lu, Z., Streets, D. G., de Foy, B., and Krotkov, N. A.: Ozone monitoring instrument observations of interannual increases in SO2 emissions from Indian coal-fired power plants during 2005-2012, Environmental science & technology, 47, 13 993–14 000, 595 https://doi.org/10.1021/es4039648, https://doi.org/10.1021/es4039648, 2013.

Lurton, T., Jégou, F., Berthet, G., Renard, J.-B., Clarisse, L., Schmidt, A., Brogniez, C., and Roberts, T. J.: Model simulations of the chemical and aerosol microphysical evolution of the Sarychev Peak 2009 eruption cloud compared

to in situ and satellite observations, Atmospheric Chemistry and Physics, 18, 3223–3247, https://doi.org/10.5194/acp-18-3223-2018, https://www.atmos-chem-phys.net/18/3223/2018/, 2018.

600 Malinina, E.: Retrieval of stratospheric aerosol characteristics from spaceborne limb sounders, PhD Thesis, University of Bremen, http://nbn-resolving.de/urn:nbn:de:gbv:46-00107153-12, 2019.

Malinina, E., Rozanov, A., Rozanov, V., Liebing, P., Bovensmann, H., and Burrows, J. P.: Aerosol particle size distribution in the stratosphere retrieved from SCIAMACHY limb measurements, Atmospheric Measurement Techniques, 11, 2085–2100, https://doi.org/10.5194/amt-11-2085-2018, https://www.atmos-meas-tech.net/11/2085/2018/, 2018.

605 Marshall, L., Schmidt, A., Toohey, M., Carslaw, K. S., Mann, G. W., Sigl, M., Khodri, M., Timmreck, C., Zanchettin, D., Ball, W. T., et al.: Multi-model comparison of the volcanic sulfate deposition from the 1815 eruption of Mt. Tambora, Atmospheric Chemistry and Physics, 18, 2307–2328, 2018.

McCormick, M. P., Lei, L., and Hill, M. T.: Early results and Validation of SAGE III-ISS Ozone Profile Measurements from Onboard the International Space Station, Atmospheric Measurement Techniques Discussions, 2019, 1–14, https://doi.org/10.5194/amt-2019-353,
610 https://www.atmos-meas-tech-discuss.net/amt-2019-353/, 2019.

Mills, M. J., Richter, J. H., Tilmes, S., Kravitz, B., MacMartin, D. G., Glanville, A. A., Tribbia, J. J., Lamarque, J.-F., Vitt, F., Schmidt, A., Gettelman, A., Hannay, C., Bacmeister, J. T., and Kinnison, D. E.: Radiative and Chemical Response to Interactive Stratospheric Sulfate Aerosols in Fully Coupled CESM1(WACCM), Journal of Geophysical Research: Atmospheres, 122, 13,061–13,078, https://doi.org/10.1002/2017JD027006, http://dx.doi.org/10.1002/2017JD027006, 2017JD027006, 2017.

615 Moussallam, Y., Rose-Koga, E. F., Koga, K. T., Médard, E., Bani, P., Devidal, J.-L., and Tari, D.: Fast ascent rate during the 2017–2018 Plinian eruption of Ambae (Aoba) volcano: a petrological investigation, Contributions to Mineralogy and Petrology, 174, 90, 2019.

NASA GES DISC: OMSO2: OMI/Aura Sulphur Dioxide (SO2) Total Column 1-orbit L2 Swath 13x24 km V003, https://disc.gsfc.nasa.gov/datasets/OMSO2_003/summary, 2020a.

NASA GES DISC: OMPS_NPP_NMSO2_L2: OMPS-NPP L2 NM Sulfur Dioxide (SO2) Total and Tropospheric Column swath orbital V2,
620 https://disc.gsfc.nasa.gov/datasets/OMPS_NPP_NMSO2_L2_2/summary, 2020b.

NASA's Earthdata: MLS/Aura Level 2 Sulfur Dioxide (SO2) Mixing Ratio V004 (ML2SO2) at GES DISC, https://search.earthdata.nasa.gov/search?p=C1251101777-GES_DISC&q=ML2SO2_004, 2020a.

NASA's Earthdata: SAGE III/ISS L2 Solar Event Species Profiles (HDF-EOS) V051, https://search.earthdata.nasa.gov/search/granules?p=C1576312558-LARC&fpj=SAGE%20III/ISS&as[project][0]=SAGE%20III/ISS&tl=1574370747!4!!, 2020b.

625 Niemeier, U. and Timmreck, C.: What is the limit of climate engineering by stratospheric injection of SO2?, Atmospheric Chemistry and Physics, 15, 9129–9141, https://doi.org/10.5194/acp-15-9129-2015, http://www.atmos-chem-phys.net/15/9129/2015/, 2015.

Niemeier, U., Timmreck, C., Graf, H.-F., Kinne, S., Rast, S., and Self, S.: Initial fate of fine ash and sulfur from large volcanic eruptions, Atmospheric Chemistry and Physics, 9, 9043–9057, http://www.atmos-chem-phys.net/9/9043/2009/, 2009.

Niemeier, U., Schmidt, H., and Timmreck, C.: The dependency of geoengineered sulfate aerosol on the emission strategy, Atmospheric
630 Science Letters, 12, 189–194, 2011.

Oman, L., Robock, A., Stenchikov, G. L., Thordarson, T., Koch, D., Shindell, D. T., and Gao, C.: Modeling the distribution of the volcanic aerosol cloud from the 1783–1784 Laki eruption, Journal of Geophysical Research: Atmospheres, 111, 2006.

Pedergnana, M., Loyola, D., Apituley, A., Sneep, M., and Veefkind, J. P.: Sentinel-5 precursor/TROPOMI Level 2 Product User ManualSulphur Dioxide SO2, 2018.

635 Pumphrey, H. C., Read, W. G., Livesey, N. J., and Yang, K.: Observations of volcanic SO$_2$ from MLS on Aura, Atmospheric Measurement Techniques, 8, 195–209, https://doi.org/10.5194/amt-8-195-2015, https://www.atmos-meas-tech.net/8/195/2015/, 2015.

Randel, W. J., Park, M., Emmons, L., Kinnison, D., Bernath, P., Walker, K. A., Boone, C., and Pumphrey, H.: Asian monsoon transport of pollution to the stratosphere, Science, 328, 611–613, 2010.

Rieger, L. A., Malinina, E. P., Rozanov, A. V., Burrows, J. P., Bourassa, A. E., and Degenstein, D. A.: A study of the approaches used to
640   retrieve aerosol extinction, as applied to limb observations made by OSIRIS and SCIAMACHY, Atmospheric Measurement Techniques Discussions, 2018, 1–21, https://doi.org/10.5194/amt-2017-446, https://www.atmos-meas-tech-discuss.net/amt-2017-446/, 2018.

S5P Data Hub: Sentinel-P Pre-Operations Data Hub, https://s5phub.copernicus.eu/dhus/#/home, 2020.

Schmidt, A., Mills, M. J., Ghan, S., Gregory, J. M., Allan, R. P., Andrews, T., Bardeen, C. G., Conley, A., Forster, P. M., Gettelman, A., et al.: Volcanic radiative forcing from 1979 to 2015, Journal of Geophysical Research: Atmospheres, 123, 12 491–12 508, 2018.

645 Seftor, C., Jaross, G., Kowitt, M., Haken, M., Li, J., and Flynn, L.: Postlaunch performance of the Suomi National Polar-orbiting Partnership Ozone Mapping and Profiler Suite (OMPS) nadir sensors, Journal of Geophysical Research: Atmospheres, 119, 4413–4428, 2014.

Siddaway, J. and Petelina, S.: Transport and evolution of the 2009 Australian Black Saturday bushfire smoke in the lower stratosphere observed by OSIRIS on Odin, Journal of Geophysical Research: Atmospheres, 116, 2011.

Smithsonian Institution: Global Volcanism Program Database, http://volcano.si.edu/search_eruption.cfm, 2019.

650 Solomon, S.: Stratospheric ozone depletion: A review of concepts and history, Reviews of Geophysics, 37, 275–316, 1999.

Solomon, S., Daniel, J. S., Neely, R. R., Vernier, J.-P., Dutton, E. G., and Thomason, L. W.: The persistently variable "background" stratospheric aerosol layer and global climate change, Science, 333, 866–870, 2011.

Stier, P., Feichter, J., Kinne, S., Kloster, S., Vignati, E., Wilson, J., Ganzeveld, L., Tegen, I., Werner, M., Balkanski, Y., Schulz, M., Boucher, O., Minikin, A., and Petzold, A.: The aerosol–climate model ECHAM5–HAM, Atmos. Chem. Phys., 5, 1125–1156, 2005.

655 Theys, N., De Smedt, I., Yu, H., Danckaert, T., van Gent, J., Hörmann, C., Wagner, T., Hedelt, P., Bauer, H., Romahn, F., Pedergnana, M., Loyola, D., and Van Roozendael, M.: Sulfur dioxide retrievals from TROPOMI onboard Sentinel-5 Precursor: algorithm theoretical basis, Atmospheric Measurement Techniques, 10, 119–153, https://doi.org/10.5194/amt-10-119-2017, https://www.atmos-meas-tech.net/10/119/2017/, 2017.

Thomason, L. and Peter, T.: SPARC Assessment of Stratospheric Aerosol Properties (ASAP), Tech. rep., SPARC, http://www.sparc-climate.
660   org/publications/sparc-reports/, 2006.

Timmreck, C.: Three–dimensional simulation of stratospheric background aerosol: First results of a multiannual general circulation model simulation, J. Geophys. Res., 106, 28 313–28 332, 2001.

Toohey, M., Krüger, K., Schmidt, H., Timmreck, C., Sigl, M., Stoffel, M., and Wilson, R.: Disproportionately strong climate forcing from extratropical explosive volcanic eruptions, Nature Geoscience, 12, 100–107, 2019.

665 Veefkind, J., Aben, I., McMullan, K., Förster, H., De Vries, J., Otter, G., Claas, J., Eskes, H., De Haan, J., Kleipool, Q., et al.: TROPOMI on the ESA Sentinel-5 Precursor: A GMES mission for global observations of the atmospheric composition for climate, air quality and ozone layer applications, Remote Sensing of Environment, 120, 70–83, 2012.

Vernier, J.-P., Thomason, L., and Kar, J.: CALIPSO detection of an Asian tropopause aerosol layer, Geophysical Research Letters, 38, 2011.

von Savigny, C., Ernst, F., Rozanov, A., Hommel, R., Eichmann, K.-U., Rozanov, V., Burrows, J., and Thomason, L.: Improved stratospheric
670   aerosol extinction profiles from SCIAMACHY: validation and sample results, Atmospheric Measurement Techniques, 8, 5223–5235, 2015.

von Savigny, C., Timmreck, C., Buehler, S., Burrows, J., Giorgetta, M., Hegerl, G., Horvath, A., Hoshyaripour, G. A., Hoose, C., Quaas, J., Malinina, E., Rozanov, A., Schmidt, H., Thomason, L., Toohey, M., and Vogel, B.: The Research Unit VolImpact: Revisiting the volcanic impact on atmosphere and climate ? preparations for the next big volcanic eruption, Meteorologische Zeitschrift, pp. –, https://doi.org/10.1127/metz/2019/0999, http://dx.doi.org/10.1127/metz/2019/0999, 2020.

675

WMO: A three-dimensional science: Second session of the commission for aerology, WMO Bull, 4, 134–138, 1957.

WMO, W. M. O.: Polar stratospheric ozone: past, present, and future, Chapter 4 in Scientific Assessment of Ozone Depletion: 2018, Global Ozone Research and Monitoring Project-Report No. 58, 2018.

Zhang, Y., Li, C., Krotkov, N. A., Joiner, J., Fioletov, V., and McLinden, C.: Continuation of long-term global SO_2 pollution monitoring

680

from OMI to OMPS, Atmospheric Measurement Techniques, 10, 1495–1509, https://doi.org/10.5194/amt-10-1495-2017, https://www.atmos-meas-tech.net/10/1495/2017/, 2017.

Zhu, Y., Toon, O. B., Kinnison, D., Harvey, V. L., Mills, M. J., Bardeen, C. G., Pitts, M., Bègue, N., Renard, J.-B., Berthet, G., et al.: Stratospheric aerosols, polar stratospheric clouds, and polar ozone depletion after the Mount Calbuco eruption in 2015, Journal of Geophysical Research: Atmospheres, 123, 12–308, 2018.